CHALMERS
UNIVERSITY OF TECHNOLOGY

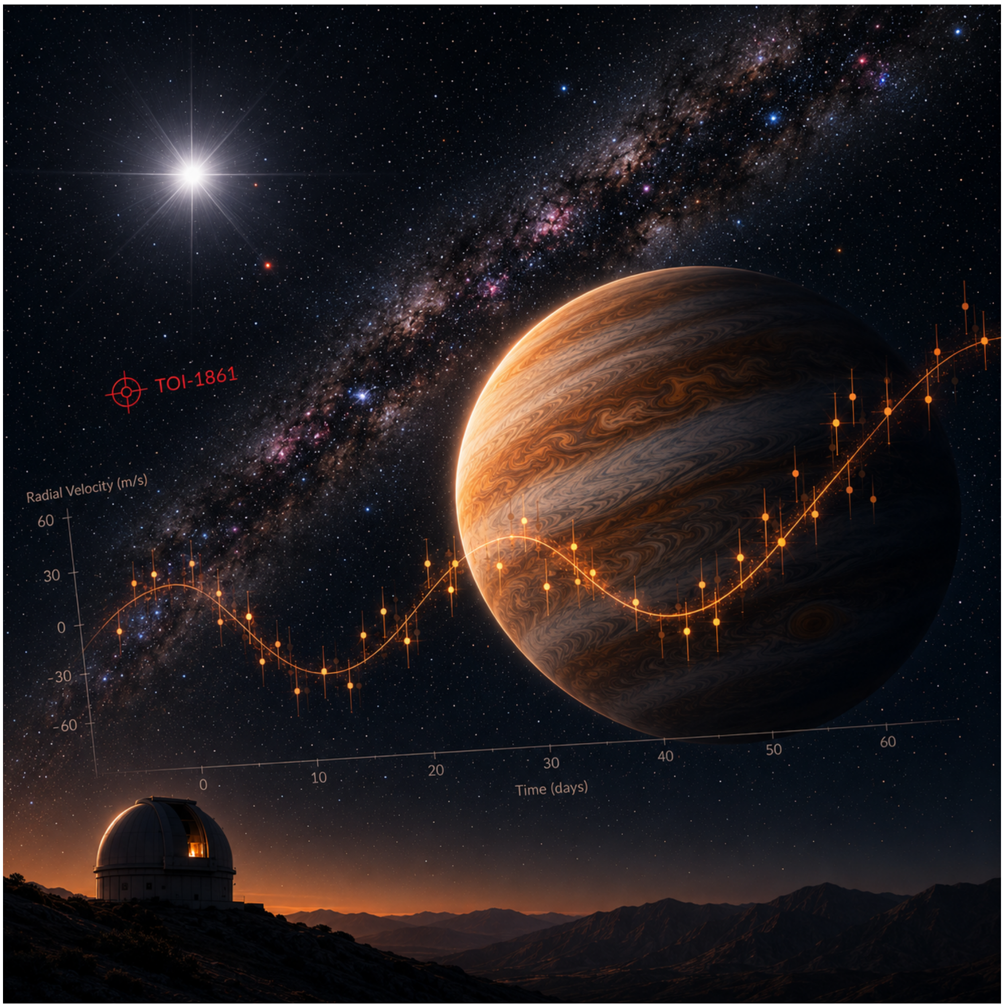

TOI-1861 b: Confirmation of a Warm Jupiter through Joint Transit and RV Modeling

Master's thesis in Physics

LINNEA LÖFVENHOLM

DEPARTMENT OF PHYSICS AND ASTRONOMY
CHALMERS UNIVERSITY OF TECHNOLOGY
Gothenburg, Sweden 2026
www.chalmers.se

MASTER'S THESIS 2026

TOI-1861 b: Confirmation of a Warm Jupiter through Joint Transit and RV Modeling

LINNEA LÖFVENHOLM

Department of Physics and Astronomy
Chalmers University of Technology
Gothenburg, Sweden 2026

TOI-1861 b: Confirmation of a Warm Jupiter through Joint Transit and RV Modeling

Supervisor and Examiner: Professor Carina Persson. Department of Physics and Astronomy. Division of Astronomy and Plasma physics.

Master's Thesis 2026
Department of Physics and Astronomy
Chalmers University of Technology
SE-412 96 Gothenburg
Sweden
Telephone +46 31 772 1000

Cover: AI-generated illustration.
Typeset in LaTeX
Gothenburg, Sweden 2026

Abstract

As of today, thousands of exoplanet candidates are waiting to be either confirmed as planets, or rejected. In this work, one of these candidates' planetary nature was confirmed through modeling both transit- and radial velocity (RV) data with the software pyaneti. The confirmed planet, TOI-1861 b, is a warm Jupiter with a mass of $1.0 \pm 0.1\,M_{\mathrm{J}}$, a radius of $1.00 \pm 0.05\,R_{\mathrm{J}}$, an eccentricity of 0.10 ± 0.02, and an orbital period of 185.6281 ± 0.0001 days. Light curves from the Transiting Exoplanet Survey Satellite (TESS) were used, in combination with RV data, created from spectra collected with the High Accuracy Radial Velocity Planet Searcher (HARPS). The model was constructed using the software pyaneti, which applies Bayesian statistics and Markov Chain Monte Carlo (MCMC) sampling to determine the planetary parameters that best reproduce the observations. In addition to confirming the planet, the fitted orbital period rules out the previously proposed orbital period of 742 days, which was based solely on transits detected in the TESS light curves. The analysis therefore demonstrates the importance of joint transit and RV modeling for resolving ambiguities caused by periodic signal aliasing.

Keywords: Exoplanet, transits, radial velocities, modeling.

Acknowledgements

This work could not have been made possible without the guidance and support from my supervisor, Professor Carina Persson. Thank you for supporting me, especially through the most challenging parts of this work. Thank you for reminding me how exciting this field is whenever I struggled to understand. And last but not least, thank you for making time for conversations about cats once in a while.

I would also like to thank Professor Malcolm Fridlund for his valuable input and discussions during this project.

To my friends and family, thank you for your endless support, and for always believing in me. Thank you for listening to me ramble on about exoplanets all the time and for your curiosity in my work.

Linnea Löfvenholm, Gothenburg, June 2026

List of Acronyms

Below is the list of acronyms that have been used throughout this thesis, in alphabetical order:

BLS	Box Least Squares
ESA	European Space Agency
ESO	European Southern Observatory
ExoCTK	Exoplanet Characterization Toolkit
ExoFOP	Exoplanet Follow-up Observation Program
FAP	False Alarm Probability
GLS	Generalized Lomb-Scargle
GP	Gaussian Process
HARPS	High Accuracy Radial Velocity Planet Searcher
MAST	Mikulski Archive for Space Telescopes
MCMC	Markov Chain Monte Carlo
PLATO	PLAnetary Transits and Oscillations of stars
RV	Radial Velocity
SERVAL	SpEctrum Radial Velocity AnaLyser
TESS	Transiting Exoplanet Survey Satellite

Notations

Below is the list of subject-specific notations used in this thesis.

$M_\odot$	Solar mass
$R_\odot$	Solar radius
$M_\oplus$	Earth mass
$R_\oplus$	Earth radius
M_p	Planet mass
R_p	Planet radius
M_J	Jupiter mass
R_J	Jupiter radius
AU	Astronomical unit ($1\,\mathrm{AU} = 1.496 \cdot 10^{11}\,\mathrm{m}$)
pc	parsec ($1\,\mathrm{pc} = 3.086 \cdot 10^{16}\,\mathrm{km}$)

Contents

1
Introduction

There are over a hundred billion stars in our galaxy. Add to this that our galaxy is but one in a sea of hundreds of billions of other galaxies, some containing even more stars than ours, and you really start to understand why astrophysicists have long expected there to be planets orbiting other stars, as the planets in our solar system do the Sun. Turning this expectation into fact was, however, no easy task. While the reasons for this are many, it is mainly due to the faint signals planets produce, and the advanced detection methods this necessitates. Most planets are hidden in the glare of their host stars and are therefore difficult, or impossible to observe directly. Even with the star's light blocked by a coronagraph, the enormous distance between us and even the nearest exoplanet makes direct imaging a challenge. Naturally, this raises the question: how do we detect exoplanets? Even though direct imaging is possible for some planets with today's technology, detection has historically been made possible by more creative means.

1.1 The history of exoplanets

The first exoplanet was discovered in 1992, when Aleksander Wolszczan and Dale Frail were actually studying irregularities in the pulsation period of the pulsar PSR B1257+12. Pulsars are essentially rapidly spinning neutron stars that emit beams of radio waves from their polar caps. As they spin, these beams become visible to us as very precise pulses. Measuring the timing of these allows us to infer movements of the pulsar, as even a small shift in its position affects the measured time of the pulse. This was precisely the case with PSR B1257+12: something caused the pulsar to wobble. In their paper from January 1992, Wolszczan and Frail presented evidence that the pulsar's wobbling was explained by the gravitational pull of at least two planets orbiting the pulsar (Wolszczan et al., 1992). This is one example of an indirect exoplanet detection method, and it is conceptually similar to one of our most powerful detection methods to date, namely the **radial velocity** (RV) method.

Three years after the first exoplanet discovery, the power of the RV-method was demonstrated when Michel Mayor and Didier Queloz published their paper, presenting the detection of 51 Peg b, a Jupiter-sized gas giant orbiting a Sun-like star with an orbital period of 4.2 days (Mayor et al., 1995). Although initially met with skepticism, this was considered a breakthrough for exoplanet research. First of all, it proved that other Sun-like stars can host planets, which challenged the assumption that our solar system was one of a kind. Additionally, it proved that planetary systems can be very much unlike our own, with gas giants in even closer orbit to their star than Mercury is to our Sun. Following this breakthrough, exoplanet research meant more than proving the existence of exoplanets. It now included both characterization of exoplanets, and understanding their formation. To this day, this remains a big part of exoplanet research. Worth mentioning is that confirming a planet goes beyond simply detecting a periodic signal. It is important to rule out other possible causes that mimic the signs of a planet, such as star spots, star pulsations, or perhaps even a stellar companion.

2

Theory

2.1 Geometry of Keplerian orbits

An orbit is the result of the gravitational force exchange between two massive bodies in motion. Planets, as well as their host star, orbit a shared center of mass, called the barycenter. If the mass of the star is much larger than that of the planet, as is often the case, the barycenter will be considerably closer to the star. Gravitational force exchange between a star and a planet results in both a larger orbit, and greater acceleration for the planet. Therefore, we often say that planets orbit their star, instead of their shared center of mass. However, it is important to think of it in the latter, more correct way in order to understand both the radial velocity method (more on this in section 2.2.1) and the geometry of planetary systems.

Kepler's three laws of planetary motion describe the orbits of planets. Kepler's first law tells us that planets have elliptical orbits, with the star at one of the foci. This means that the distance between the planet and the star varies throughout the orbit. Although all planets have elliptical orbits, they are far from identical in shape and size. The semi-major axis, a is half the length of the longest line in an ellipse, and it is a measure of the size of an orbit. It relates to the orbital period, P of an orbit through Kepler's third law (Perryman, 2018). Under the assumption that $M_\star \gg M_\mathrm{p}$, Kepler's third law is:

$$P^2 = \frac{4\pi^2}{GM_\star}a^3 \tag{2.1}$$

The orbital period of a planet is the time for completion of one orbit around the barycenter. According to Kepler's third law, both a and P are measures of the size of an orbit.

Furthermore, the elongation of an orbit is quantified by its eccentricity, $0 \leqslant e < 1$. If $e = 0$, the orbit is circular, which is a special case of an ellipse. Conversely, if $e = 1$, the orbit has the shape of a parabola, and thus the body is not gravitationally bound to the star. The shape of an orbit is far from constrained by eccentricity alone. Because planetary systems exist in three-dimensional space, an orbit is also defined by its orientation. When we observe a star, our view-point is limited by our position in space. Our field of view is called the reference plane. It is always orthogonal to the line of sight, which is the direction in which we are observing. The inclination, $0° \leqslant i \leqslant 180°$ of an orbit is the angle between the reference- and the orbital plane. If $i = 0°$ or $i = 180°$, the orbital plane coincides with the reference plane, and we are observing it face-on. If we are observing it edge-on instead, it has $i = 90°$ and the orbital plane is orthogonal to the reference plane.

The point on an orbit where a planet is furthest from its star is called the apocenter. Similarly, the point where the planet is closest to its star is called the periastron. The argument of periastron, ω is the angle between the ascending node and the periastron. Thus, ω describes the orientation of the orbit within the orbital plane. There are additional angular parameters to completely describe the orbit, such as the longitude of the ascending node, Ω and the true anomaly, $\nu(t)$. Figure 2.1 depicts a three-dimensional Keplerian orbit.

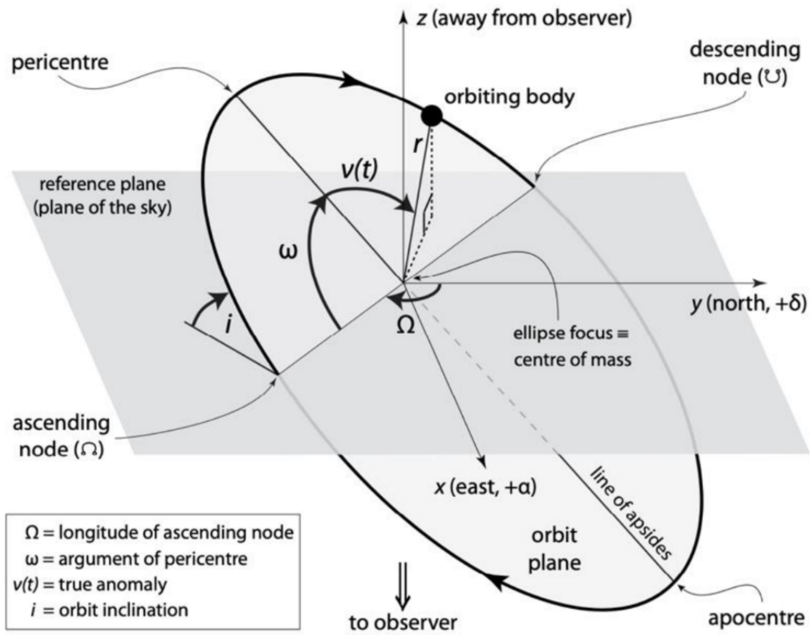

Figure 2.1: The orbit of a planet is elliptical and can be described by its shape, size and orientation in three-dimensional space. In turn, the orbit determines what is observed from our point of view (Perryman, 2018).

The shape, size and orientation of a planet's orbit directly affect what can be observed from our position in space, and thus, which methods are suitable to carry out observations. For example, the RV method is not suitable for planets with $i \approx 0°$ due to the small radial velocity component such inclinations induce. Additionally, face-on orbits like these make transit photometry impossible simply because planets in such orbits will not be seen transiting the stellar disk from our line of sight.

2.2 Exoplanet Detection

As of today, more than 6000 exoplanets have been confirmed, as listed on NASA exoplanet archive[1]. The planet confirmations are thanks to a variety of different detection methods. Common detection methods include the radial velocity (RV) method, transit photometry, transit timing variations, direct imaging and microlensing. As shown in figure 2.2 and figure 2.3, the methods that have resulted in the most detections are transit photometry, and the RV method. Together, these two methods have contributed to over 90 % of exoplanet detections. The other methods mentioned above, and included in the figures will not be covered in further detail in this report.

As seen in Figure 2.2 and Figure 2.3, planets of the same nature as our solar system's planets are seldom detected with the methods and instruments available to us today. Their long orbits or low masses result in faint signals, and to effectively detect planets like these with either the transit- or RV method we need telescopes or spectrographs with higher sensitivities. To this day, no planet like Earth has been detected orbiting a Sun-like star, but with new missions, such as the PLAnetary Transits and Oscillations of stars (PLATO) space mission, with a planned launch in 2027, we are progressing towards possibly detecting more Earth-like planets.

[1]NASA Exoplanet Archive: `https://exoplanetarchive.ipac.caltech.edu/`

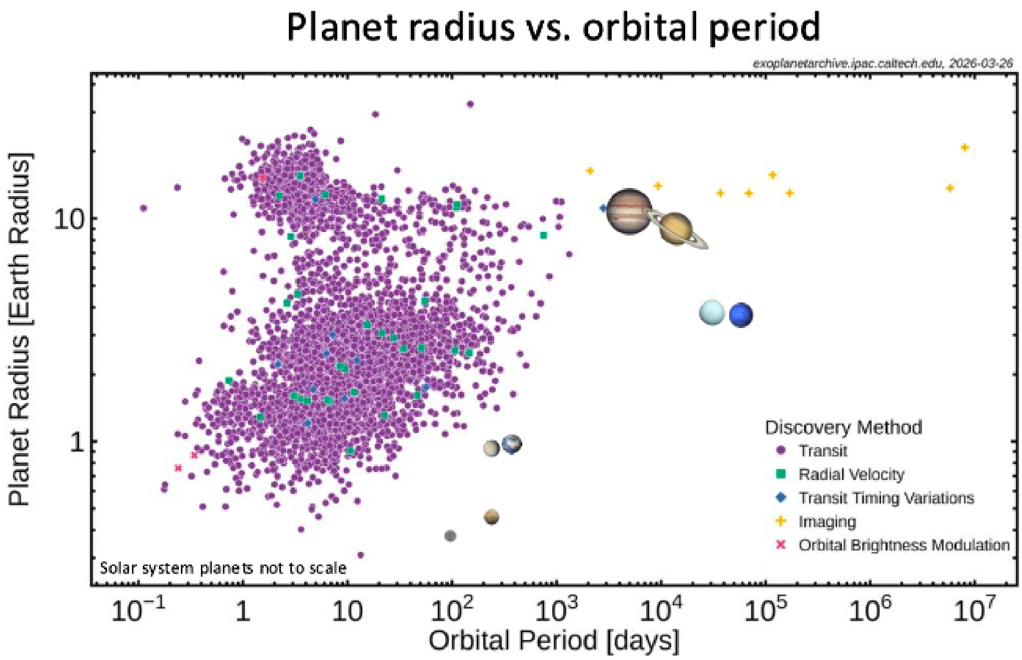

Figure 2.2: The number of detected planets by each method, plotted in a radius-period diagram. The figure is adapted from NASA exoplanet archive.

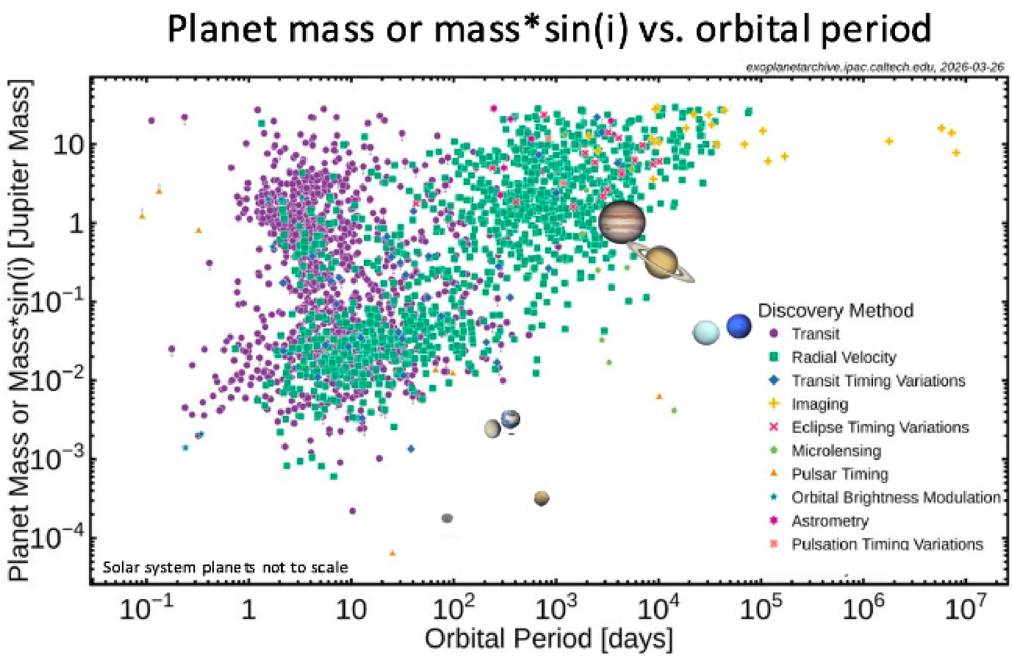

Figure 2.3: The number of detected planets by each method, plotted in a mass-period diagram. The figure is adapted from NASA exoplanet archive.

2.2.1 The radial velocity method

The Radial Velocity (RV) method is an indirect planet detection technique. It is based on measuring Doppler shifts of spectral lines in the star's spectrum. Due to the wave-like properties of light, the observed wavelength will be shorter if the source is moving towards us. Conversely, the wavelength will be longer if it moves away from us. This change in wavelength is the Doppler shift, and how it relates to the motion of the star is illustrated in figure 2.4.

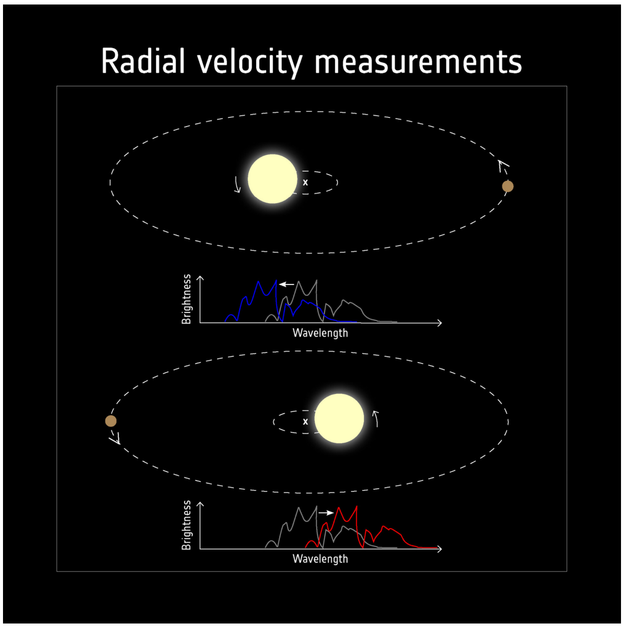

Figure 2.4: The Doppler shift of a star's spectrum as it moves radially relative to us. A radial velocity towards us shifts wavelength towards the red end of the spectrum, and towards the blue end if the star is moving away from us. Image credits: European Space Agency (ESA).

To measure this, a spectrum must first be obtained. This is done with high precision spectrographs, such as the High Accuracy Radial Velocity Planet Searcher (HARPS) for example. Spectrographs can measure the intensity of light from a star as a function of wavelength. In other words, the spectrum of a star, which is an intensity distribution over an interval of wavelengths. A spectrum can contain both a continuous distribution of intensity, known as a continuum, and narrow lines of intensities at specific wavelengths. These spectral lines act as fingerprints for ions, atoms and molecules and appear at well-documented wavelengths. It is from the Doppler shift of these spectral lines that one can calculate the radial velocity of the star as it orbits the center of mass. Specifically, the momentary radial velocity, v_{R} relates to the Doppler shift as

$$v_{\mathrm{R}} = \frac{c\,\Delta\lambda}{\lambda 0} = \frac{c\,(\lambda_{\mathrm{obs}} - \lambda_0)}{\lambda_0}, \tag{2.2}$$

where $\Delta\lambda$ is the Doppler shift, namely the difference between the rest wavelength of the spectral line λ_0, and the observed wavelength λ_{obs} (Perryman, 2018). Relativistic effects have been neglected in the formula. In order to extract more information about the planet, it is necessary to know how the radial velocity changes periodically over time. In other words, a RV time series is required. Thus, the RV method involves repeated observations, as one spectrum corresponds to one RV value - the momentary radial velocity.

A periodic RV of a star is indicative of at least one other massive body present in the star's proximity, causing it to wobble. However, the nature of this massive body is not automatically inferred. It could be a planet, brown dwarf, or a stellar companion. It is also possible that it is an effect caused by the star's intrinsic behaviors, such as stellar pulsations, and not an additional body at all. To determine if the RV is actually caused by a planetary companion, further analysis is needed. The derived lower mass limit of the hypothetical body, as well as the shape of the spectral lines, aids in the process of ruling out both stellar-like companions, and star activity as underlying causes of the RV.

If a Keplerian model is fitted to the RV time series, key orbital observables of a planet can be extracted directly, such as the orbital period, P, eccentricity,e, semi-amplitude, K, and argument of periastron, ω. Additionally, a systemic velocity, γ can be obtained from the fit. The systemic velocity is the velocity of the star system relative to the solar system. The systemic velocity is usually subtracted from obtained RV values in order to visualize the periodic variation caused by the wobble of the star. With the systemic velocity removed, the semi-amplitude is the maximum value of the radial velocity for the star. In a RV time series, containing a periodic signal, the RV semi-amplitude is half of the total amplitude. The semi-amplitude can be expressed as

$$K = \left(\frac{2\pi G}{P}\right)^{1/3} \cdot \frac{M_{\mathrm{p}} \sin(i)}{(M_\star + M_{\mathrm{p}})^{2/3}} \cdot \frac{1}{\sqrt{1-e^2}}. \tag{2.3}$$

Moreover, if the stellar mass $M_\star$ is well-known, the lower mass limit of the planet: $M_{\mathrm{p}} \sin(i)$ can be derived (Perryman, 2018). Assuming that $M_\star \gg M_{\mathrm{p}}$, equation (2.3) can be rearranged to obtain an expression for the lower mass limit of the planet instead:

$$M_{\mathrm{P}} \sin(i) = K \cdot \sqrt{1-e^2} \cdot M_\star^{2/3} \left(\frac{2\pi G}{P}\right)^{-1/3}. \tag{2.4}$$

If the inclination (i) of the orbital plane is known, the planet's mass is obtained instead of merely a lower mass limit. The inclination is not extracted from RV measurements, but can be determined through transit photometry. This is discussed in further detail in section 2.2.2. The mass of the planet is necessary to determine the bulk density of the planet. Thus, the RV method is a valuable tool not only for planet detection, but for planet characterization as well.

The RV method has limitations. It is sensitive to planets that yield a large wobble of the star because it corresponds to a stronger signal, or specifically, a larger semi-amplitude. Therefore, it can not be used on planets orbiting a star in an orbital plane that is orthogonal to the line of sight ($i = 0°$), as the motion will never be radial relative to us in such an orbit. The semi-amplitude in the RV time series decreases with decreasing inclination of the orbital plane, as inclination is defined such that a parallel orbital plane corresponds to $i = 90°$. Furthermore, massive short-period planets create a larger wobble of the star, and thus the RV method is biased towards this category of planets (Georgieva, 2023). Additionally, the RV method is more sensitive to planets orbiting low-mass stars, since lower stellar masses allow planets to induce larger velocities.

2.2.2 The transit method

The transit method has been highly successful because it enables large photometric surveys and provides periodic signals from which orbital periods, planetary radii, and orbital inclinations can be derived. Monitoring many stars simultaneously increases the chance of detecting transiting planets, since only systems with orbital planes closely aligned with our line of sight produce observable transits.

If a planet's orbital plane aligns with our line of sight, the planet can be indirectly observed as it transits the star in its orbit. In reality, this is observed as a decrease in the measured light from the star, as the planet blocks parts of it. Figure 2.5 is a schematic of a planet transiting its host star. In the figure, the number 1 marks the beginning of the transit event, and the beginning of the ingress. When the whole planet is in front of the star, the ingress ends. At this time, the planet is approaching its midpoint. As the planet starts to exit, the egress begins. This is marked by the number 3 in the figure. When the planet has exited fully, the egress as well as the transit event is over. The ingress and egress are present due to a phenomenon called limb darkening. It is an effect from the star, which appears brighter closer to its center compared to its edges.

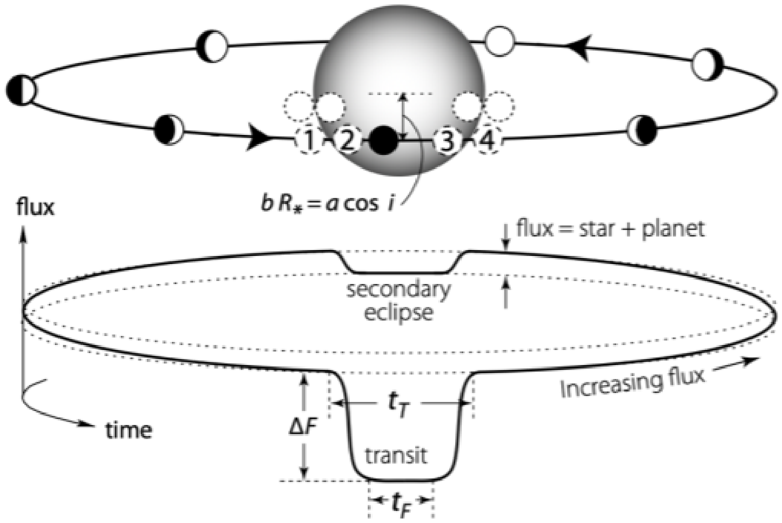

Figure 2.5: Schematic of a transit (Perryman, 2018). It depicts both the planet orbiting the star, and the corresponding decrease of the measured light from the host star.

The decrease of the measured light corresponds to the transit depth. The transit depth, ΔF, depends on the ratio between the radius of the star and the radius of the planet. Neglecting limb darkening, the transit depth relates to the planet-to-star radius ratio as, $\Delta F = (R_\mathrm{p}/R_\star)^2$ (Perryman, 2018). By measuring two consecutive transits, the orbital period of the planet can be derived. If the transit midpoints occur at t_1 and t_2, then the orbital period is $P = t_2 - t_1$. If the orbital period is known, future transits can be predicted, which facilitates follow-up transit observations. Furthermore, the shape of the transit and the transit duration, t_τ, constrains geometric parameters such as the scaled semi-major axis, a/R*, inclination, i and impact parameter, b. The impact parameter is the projected distance between the planet and star centers during mid-transit. It can be expressed as

$$b = \frac{a\cos(i)}{R_\star}. \tag{2.5}$$

2.2.3 The power of joint transit and RV modeling

As previously mentioned, both RV and transit observations provide information about the planetary parameters. However, combining both RV and transit observations yields results of higher value. For example, RV measurements alone can constrain the minimum planetary mass, $M_\mathrm{p}\sin(i)$, but can not determine the true planetary mass due to the unknown orbital inclination. Transit observations, on the other hand, constrain the inclination through the geometry of the transit. Thereby, the combination of RV and transit data allows the planetary mass to be determined. This is particularly important because transit data also provides the planet-to-star radius ratio, and the planetary radius if the stellar radius is known. Together, planetary mass and radius yield the bulk density of the planet, which enables a first insight into the composition, and thus the character of the planet (Georgieva, 2023).

In addition to this, joint RV and transit modeling breaks parameter degeneracies. For example, even if multiple planet transits have been observed, estimating the orbital period can still be challenging. Although two consecutive transit events can yield the orbital period, this in itself poses a challenge for long-period planets. Through joint transit and RV modeling, the orbital period can be inferred despite of any missed transit events in the data. Consequently, joint transit and RV modeling of a planet candidate is sufficient to confirm the planetary nature of the candidate.

2.3 Exoplanet categorization

Due to the diversity of exoplanets and planetary systems, no single detection method is equally sensitive to all types of planets. Transit photometry favors planets in short-period orbits with orbital planes aligned close to our line of sight. Radial velocity observations are most sensitive to massive planets and can detect non-transiting planets, including longer-period planets, but are more challenging for low-mass planets because their velocity signals are small. Detection bias makes it necessary to distinguish between what is frequently detected, and what is frequently occurring. What is the most common planet type? To answer that question, let's begin with an introduction to the different types of planets found as of yet.

Planets are characterized by their properties, such as their mass and radius. Based on size, a planet can be categorized as one of the following (Fulton et al., 2017; Petigura et al., 2022):

- Earth-sized ($< 1.25\,\mathrm{R}_{\oplus}$.)
- Super-Earth-sized ($1.25 - 1.8\,\mathrm{R}_{\oplus}$)
- Sub-Neptune-sized ($1.8 - 3.5\,\mathrm{R}_{\oplus}$)
- Neptune-sized ($3.5 - 6\,\mathrm{R}_{\oplus}$)
- Jupiter-sized ($6 - 15\,\mathrm{R}_{\oplus}$).

However, no strict definition is established, and the intervals vary in different literature. Similarly, planets can be characterized further if their orbital period is taken into account. Among such categories of exoplanets, warm Jupiters are the most relevant class for this work. They are Jupiter-sized planets with orbital periods between $10 - 200\,\mathrm{days}$ (Dawson et al., 2018).

Furthermore, mass and radius determine the bulk density of a planet. The bulk density is important because it hints at the planet's composition (de Pater et al., 2015). When a planet forms, its core forms first. If there is a sufficient amount of solid materials available at the site of formation, the core will accrete enough mass to gravitationally attract substantial amounts of gas (mainly helium and hydrogen), creating a gaseous envelope. This process leads to the formation of gas giants. They possess big radii relative to their mass, and therefore have lower bulk densities than rocky planets. In other words, small planet bulk densities of approximately $1\,\mathrm{g/cm^3}$ are indicative of a composition of materials with small mean molecular weight (de Pater et al., 2015). However, bulk density is not enough to fully constrain the composition of a planet. An example of this can be found in our own solar system, where the gas giant Jupiter has a higher bulk density compared to the ice giant Uranus. Their bulk densities are $1.32\,\mathrm{g/cm^3}$ and $1.21\,\mathrm{g/cm^3}$ respectively (Nordling et al., 2006). While ice giants also contain high amounts of hydrogen and helium, they differ from gas giants in that they also contain volatiles like water, ammonia and methane. Using spectroscopy for complementary analysis of a planet's atmosphere can yield better constraints on planet composition and is a valuable tool for categorizing planets.

By characterizing detected exoplanets, and statistically correcting for inevitable detection biases, the question of what the most common exoplanet type is has largely been answered. Current exoplanet surveys show that the most common types of planets are super-Earths and sub-Neptunes. This makes our solar system uncommon, as it does not contain any planets of these categories. However, if systems like ours occur frequently or not ultimately remains to be answered (de Pater et al., 2015).

2.4 Periodograms

A periodogram is a mathematical tool used for identifying periodic signals of a time series. In this work, periodograms were applied to RV data to identify candidate periodicities. A periodogram displays frequency, or equivalently period, on the horizontal axis and a quantity commonly referred to as power on the vertical axis. The exact definition of the y-axis depends on the implementation of the periodogram, but it can be interpreted as a measure of how strongly a periodic signal of a given frequency is present in the data. A strong periodic signal indicates a candidate periodic signal.

Periodogram methods are closely related to Fourier analysis. In Fourier analysis, a periodic signal is interpreted as the sum of sinusoidal signals of different frequencies. A Fourier transform transforms a signal from the time domain to the frequency domain. The time domain illustrates how the signal changes over time, while the frequency domain reveals the periodic components of the signal, if there are any.

There are different types of periodograms, such as the Generalized Lomb-Scargle (GLS) periodogram and the Box Least Squares (BLS) periodogram. The former is a used to identify sinusoidal signals in unevenly-spaced time series, which makes it a suitable choice for RV time series (Hatzes, 2019). Additionally, GLS periodograms take varying uncertainties in the data set into account by giving greater weight to more precise measurements. In this work, a GLS periodogram was created for the RV time series, and is presented in Figure 5.2.

Although transit signals are periodic, they are not sinusoidal. Consequently, GLS periodograms are not optimal to search for periodic signals from transits in light curves. Instead, BLS periodograms are more commonly used for this purpose. The BLS method works by iteratively fitting box-shaped transit models to the light curve, and calculating how well it fits. Strong peaks in the resulting BLS periodogram indicate candidate periods for which a box-shaped transit model provides a comparatively good fit to the light curve.

It is not always straight forward to evaluate the nature of a periodogram peak. Firstly, if there are data gaps, or if the data is unevenly spaced, periodograms will have a feature referred to as alias peaks at frequencies that are not corresponding to a signal in the data (Hatzes, 2019). In astronomy, data is seldom evenly spaced, due to telescope schedules, moon contamination, weather conditions etc. Thus, alias peaks are a common feature in periodograms derived from astronomical data. The frequencies of alias peaks depend on the frequency of the real signal as well as the sampling frequency: $f_{\text{alias}} = f_{\text{true}} \pm n \cdot f_{\text{sample}}$. Secondly, if a signal is not perfectly sinusoidal, it will give rise to harmonic peaks in a periodogram. The frequencies of harmonic peaks are integer multiples of the true signal's frequency. Harmonics can be recognized by the harmonic pattern in which they occur, centered around the real frequency. In general, further diagnostics is needed to distinguish periodic signals from aliasing, harmonics or noise. For example, examination of the window function is often required (Hatzes, 2019). Features such as harmonics and alias peaks create the need for a quantitative estimate of a peak's significance. The False Alarm Probability (FAP) provides such a measure. A low FAP value represents a statistical significance relative to the null-hypothesis, but does not in itself exclude activity, systematic effects or aliasing as causes to the peaks.

2.5 Bayesian inference and MCMC sampling

Transit- and RV data can be described by a model, consisting of a set of model parameters. The combination of parameter values that best describes the data can be determined statistically. However, different parameter combinations may provide solutions of similar plausibility. Thus, one would like to determine not only one combination of parameter values that fit the observations, but rather a probability distribution covering many different combinations of parameter values. In Bayesian inference, this distribution is known as the posterior distribution, or simply the posterior. Bayesian inference is a statistical framework based on Bayes' theorem. Mathematically, Bayes' theorem can be expressed as

$$P\left(\theta|D\right) \propto P\left(D|\theta\right) P\left(\theta\right), \tag{2.6}$$

where $P\left(\theta|D\right)$ is the posterior of the model parameters, θ, given the observational data, D (Perryman, 2018). Furthermore $P\left(\theta\right)$ is the prior probability, or simply the prior. The prior constitutes any previous knowledge of the model parameters before taking the data into account, and can therefore be more or less informative. There are many different types of priors, but two types are especially significant for this work, namely the uniform prior and the gaussian prior. A uniform prior assigns equal probability to all parameter values in a specified interval. A gaussian prior assigns the highest probability to a given mean value, and probabilities decrease with distance from the mean, creating a gaussian (bell-shaped) curve. Additionally, $P\left(D|\theta\right)$ is the likelihood. The likelihood describes how likely the observed data is for a given set of model parameters, while the posterior describes how probable the set of parameter values is after taking into account both the likelihood and the prior.

For models with many free parameters, obtaining the posterior distribution analytically can be too challenging. Instead, numerical methods have been developed to sample the posterior distribution. One such method is Markov Chain Monte Carlo (MCMC) sampling (Perryman, 2018). MCMC is a combination of two different techniques. The Monte Carlo technique involves approximating a distribution's properties by examining samples of it, selected at random. Markov Chain is the technique implemented for the selection of the samples. With a Markov Chain approach, sampling is sequential and the next sample step always depends on the previous one. The entire sampling sequence is called a chain, and one chain finishes after a set number of iterations. Because the first sample is always random, the sampling is improved by initiating more than one sequence simultaneously. Every sequence evolves independently and the number of initiated sampling sequences is referred to as the number of walkers. If the chains converge, meaning they sample the same region of parameter space regardless of their initial position, the posterior can be regarded as reliable.

3

Data

3.1 HARPS

The High Accuracy Radial Velocity Planet Searcher (HARPS) is a spectrograph installed at the 3.6-m telescope at the La Silla observatory in Chile. The La Silla observatory is owned by the European Southern Observatory (ESO) and extensive information about HARPS can be found on ESO's website[1]. HARPS was installed in 2003, and has since contributed to numerous major exoplanet discoveries, including the detection of several low-mass planets. It's spectral range is $378 - 691\,\mathrm{nm}$. As the name suggests, HARPS can yield RV measurements of exceptionally high accuracy. With a measured spectral resolution of $R = 115000$, and through combining information from as many spectral lines as possible, HARPS can reach a precision corresponding to RV:s on the order of $1\,\mathrm{m/s}$. To put that into perspective, HARPS can measure the radial velocity of a star, even if that velocity is small enough to be comparable to the average human walking pace.

The HARPS data for TOI-1861 was collected from ESO's science archive facility[2], where 31 HARPS spectra are publicly available for use at the time of writing (June, 2026). The 31 spectra used in this work are distributed unevenly between 2021 and 2023, across a total time span of 26 months. The temporal data distribution can be seen in Figure 5.4.

Although HARPS is designed and installed in a vacuum cover to minimize effects from air pressure, temperature and humidity to increase stability and decrease unwanted effects from its surroundings, environmental factors will affect the measurements regardless. Therefore, quantities such as air mass, humidity, temperature and wind direction are monitored during HARPS measurements, and can be utilized to perform a quality check of the measurement conditions.

[1] ESO's website: `https://www.eso.org/public/`

[2] The ESO science archive facility: `https://archive.eso.org/cms.html`

3.2 TESS

The Transiting Exoplanet Survey Satellite (TESS) (Ricker et al., 2015) is a space telescope. It was launched into orbit on the 18th of April in 2018. The main objective for TESS was to survey bright stars across 85% of entire sky over a period of two years, in order to detect transiting exoplanets, including Earth-sized ones. TESS observes the sky one sector at a time, for 27.4 days each. 85% of the sky is surveyed by 26 observation sectors in total. Parts of the sky overlap in different sectors, especially closer to the poles, and are thus being observed more frequently. This increases the observation baseline, which makes it possible to detect more transits of long-period planets in these regions of the sky. The sector-wise observation technique of TESS introduces the risk of missing transit events. If observed transit events are confirmed to be consecutive, the orbital period can be determined directly. However, missed transit events between two observed ones create an orbital period ambiguity. Furthermore, TESS completed its two year plan, and has since continued to observe the sky sector-by-sector. Doing so enables even more transit detections, especially of transiting planets with larger orbital periods than 27.4 days.

TESS can measure light of wavelengths between $600 - 1000\,\mathrm{nm}$ (Ricker et al., 2015), which corresponds to optical light and near-infrared radiation. TESS has the photometric precision to detect planets with smaller radii than Earth's orbiting smaller dwarf stars.

For TOI-1861, 10 TESS light curves with a cadence of 120 seconds were collected from the Mikulski Archive for Space Telescopes (MAST)[3] archive, which is an online repository for astronomical data from missions such as TESS. A 120 seconds cadence indicates that consecutive data points are separated by two minutes. The collected light curves belong to the following TESS sectors, in numerical order: 11, 12, 13, 38, 39, 65, 66, 67, 93, and 94. This corresponds to an unevenly spaced sample over a total time span of approximately 6 years.

[3]MAST's webpage: `https://archive.stsci.edu/`

4

Method

4.1 Target Selection

TOI-1861 was considered a suitable candidate for this work because it met different selection criteria. Two of these criteria involved having at least one TESS planet candidate, and a sufficient amount of available HARPS spectra. There is no well-defined lower limit for the amount of spectra needed to perform a successful RV analysis, resulting in a planet detection, but ideally the number of spectra, and their temporal distribution, should correspond to a sufficient phase coverage. TOI-1861 had 31 HARPS spectra available on ESO:s science archive facility, and one TESS planet candidate on NASA exoplanet archive.

In addition to this, another selection criterion was that the light curves should contain at least two observed transits. Without this criterion, the transit side of the modeling can not aid in the process of determining an orbital period, which is a key parameter in confirming a planetary candidate. In TOI-1861:s case, ten TESS light curves were available, containing a total of three transit events.

Furthermore, brighter stars, as seen from Earth, allow for RV measurements with higher signal-to-noise ratios. On NASA exoplanet archive, TOI-1861 has a TESS magnitude of $9.9486 \pm 0,006$, an effective temperature of $T_{\text{eff}} = 5490 \pm 148.2\,\text{K}$, and a distance of $135.758\,\text{pc}$ to Earth, which makes TOI-1861 a bright Sun-like star, and thus a suitable target for RV analysis. Spectra from Sun-like stars also contain many, narrow spectral lines due to properties like their effective temperature and rotation speed, and this allows for more precise RV measurements.

An additional selection criterion, to ensure a sufficient signal-to-noise ratio, was a transit depth greater than 1000 ppm. TOI-1861 has a listed transit depth of approximately 8486 ppm on NASA exoplanet archive.

4.2 Detrending a light curve

The ten TESS light curves for TOI-1861 were downloaded from MAST using the Python package Lightkurve[1]. Lightkurve is an open-source tool for downloading, processing and analyzing light curves (Lightkurve Collaboration, 2018). Lightkurve was also used to normalize the available light curves.

Due to the presence of long-term trends, unrelated to the transit signal, the light curves have to be detrended. The python package Citlalicue[2] is used for this purpose. Citlalicue uses Gaussian Process (GP) regression to model and remove both long-term trends and correlated variability in light curves (Barragán, 2022). Regarding the GP kernel, the Matérn 3/2 kernel is used in this work, because it allows moderately smooth variability to be modeled, which is suitable for TESS light curves. First of all, the transit events need to be identified by Citlalicue, because they will be masked to avoid being affected by the detrending process. To identify the transit events, Citlalicue is given previously derived values for the transit midpoint, orbital period, scaled semi-major axis, impact parameter, planet-to-star radius ratio, and limb darkening coefficients. This allows the transits to be masked. The width of the transit masks are based on the transit duration, with an additional margin of a few minutes. The transit duration is 6.5744 hours and thus, the width of the transit masks are set to 6.7744 hours. To detrend the light curves, the GP model is optimized iteratively, using 3σ clipping, meaning data points deviating by more than three standard deviations from the model are treated as outliers and removed. Afterwards, the model is removed, resulting in a detrended version of the light curve. Additionally, all data points more than 6 hours away from each transit were cut to reduce the computational time of the upcoming modeling process. Finally, all sectors were stitched together, resulting in Figure 5.1.

4.3 Extracting RV from spectra

A total of 31 HARPS spectra were retrieved from the ESO Science Archive Facility. To calculate an RV value from each spectrum, a python package called SpEctrum Radial Velocity AnaLyser (SERVAL)[3] (Zechmeister et al., 2018) was used. SERVAL utilizes least-squares fitting. It constructs a high signal-to-noise template spectrum from the given spectra. Following this, SERVAL matches every spectrum to the template by measuring the shift between it and every individual spectrum. SERVAL then calculates the RV value from the relative Doppler shift between the spectrum and the tem-

[1]Lightkurve on GitHub: `https://github.com/lightkurve/lightkurve`
[2]Citlalicue on GitHub: `https://github.com/oscaribv/citlalicue`
[3]SERVAL on GitHub: `https://github.com/mzechmeister/serval`

plate. Additionally, SERVAL analyzes the wavelength dependence of the measured RV signal, as well as the properties of the spectral lines to derive values for stellar activity indicators, which are features in spectra that can be used to identify stellar activity. Examples of such indicators that SERVAL provides are chromatic index (CRX), differential line width (dLW), the hydrogen-alpha line (Hα), and the sodium D lines: NaD1 and NaD2 (Zechmeister et al., 2018). In short, the CRX is a measure of how dependent the RV signal is on wavelength. Doppler shifts induced by an orbiting planet are expected to be wavelength-independent. If a dependence between the measured RV signal and wavelength is found in a star's spectrum, it can indicate stellar activity, such as star spots. The differential line width is a measure of variations in spectral line width, and a correlation between dLW and RV can indicate stellar-activity-induced RV variations, caused by pulsations for example. Regarding the Hα line as well as NaD1 and NaD2 lines, SERVAL analyzes the temporal variations of the strength of these spectral lines. A correlation between these variations and RV variations can suggest that the RV variations may be related to magnetic stellar activity.

4.4 Finding periodic signals

GLS periodograms were calculated, both for the RV values, and for the activity indicators CRX, dLW, Hα, NaD1, and NaD2. The periodograms were calculated using the LombScargle-implementation in the Python package Astropy. The uncertainties for both the RV and the stellar activity indicators were taken into account in the calculation. The periodograms were evaluated over a broad range of periods. Although the search grid was extended to long periods, the effective sensitivity is constrained by the observational baseline and temporal sampling of the data.

The activity indicator periodogram indicates whether a periodic signal is caused by stellar activity or not. If a statistically significant peak is present with the same period in both the RV- and the activity indicator periodogram, the signal could be the result of stellar activity, and not of a planet with that period. FAP levels of 1% and 0.1% were calculated to assess the statistical significance of prominent peaks in the periodograms.

In order to search for additional signals, a Keplerian model with a signal at the same period as the most prominent peak at $P = 185.6\,\text{days}$ was fitted to the RV time series and subtracted from the data. After this, a new periodogram was computed based on the residuals, in which no new peaks were revealed. This is the periodogram in the bottom panel in Figure 5.2.

4.5 Modeling in pyaneti

The Python package pyaneti[4] was used to jointly model the RV and transit data for TOI-1861, using a Keplerian model for the HARPS data and a transit model for the TESS data. Pyaneti implements MCMC sampling to estimate the Bayesian posterior distributions of model parameters based on the likelihood function and user-defined priors (Barragán et al., 2019). Previous knowledge about expected parameter ranges and values determines the type of prior applied. Although pyaneti can implement many different types of priors, only uniform and gaussian priors were used. Uniform priors were used in cases where a plausible interval for a parameter was the extent of our previous knowledge. For example, due to a lack of previously derived values, a broad uniform prior was applied for the impact parameter. Additionally, uniform priors were applied to parameters like mid-transit time, T_0, and the planet-to-star radius ratio, $R_\mathrm{p}/R_\star$ for which a first estimate could be done based on listed values on the Exoplanet Follow-up Observation Program (ExoFOP)[5] website. A uniform prior was applied for the orbital period as well, based on the prominent peak in the RV periodogram, see Figure 5.2.

Gaussian priors on the other hand were applied in more informed cases. A gaussian prior is to be used for a parameter if an independent estimation and uncertainties can be found for it. For example, gaussian priors were used for the parameterized limb darkening coefficients, q_1 and q_2, since values could be calculated for the limb darkening coefficients u_1 and u_2, using an interactive application of Exoplanet Characterization Toolkit (ExoCTK)[6]. Pyaneti uses the parameterizations for the limb darkening coefficients proposed by Kipping (2013) by default, so the following relations were used:

$$q_1 = (u_1 + u_2)^2 \text{ and } q_2 = \frac{u_1}{2(u_1 + u_2)}. \tag{4.1}$$

Furthermore, a gaussian prior was applied for the stellar density, $\rho_\star$, based on independently estimated stellar parameters. A parametrization of the eccentricity and argument of periastron proposed by Anderson et al. (2011) was adopted, and a gaussian prior was applied. Additionally, the Gaussian prior on the Doppler semi-amplitude was chosen based on an approximate amplitude observed in the RV time series, providing an informed initial estimate while allowing moderate variation during sampling.

For a full list of assigned priors in the pyaneti modeling, see Table 5.1. Furthermore, pyaneti utilizes stellar parameters, such as effective temperature,

[4] pyaneti on GitHub: `https://github.com/oscaribv/pyaneti`

[5] ExoFOP: `https://exofop.ipac.caltech.edu/tess/`

[6] ExoCTK limb darkening coefficients calculator:
`https://exoctk.stsci.edu/limb_darkening?utm_source=chatgpt.com`

stellar mass and stellar radius, together with their associated uncertainties, to calculate planetary properties, which are included in the list of derived parameters in Table 5.1. ExoFOP was used to obtain the stellar parameters for TOI-1861.

For the MCMC sampling, both the number of iterations and the number of independent Markov chains were chosen to be 500. The numbers need to allow for a sufficient sampling of the parameter space, while still maintaining computational feasibility. Pyaneti makes a convergence assessment using the Gelman-Rubin criterion (Barragán et al., 2019), which compares the variance within and between chains. How frequently pyaneti performs a convergence test is specified by the user. In this work, a convergence test was evaluated every 5000 iterations. Additionally, pyaneti lets the user decide if an additional RV jitter term or transit jitter term should be included in the model to account for additional noise with regard to the RV- or transit uncertainties. No additional jitter term was included for the transit data in this work. However it was included for the RV data. Moreover, pyaneti includes the systemic velocity in the model by default.

5
Results

Figure 5.1 shows the temporal spacing of the three observed transits, after stitching, normalizing, cutting, and detrending the TESS light curves. The data points are given in blue, while the fitted model is given in black. Every vertical line in the model indicates a transit event predicted by the joint transit and RV model. The model's orbital period is $P = 185.628$ days. All available TESS data are not depicted in Figure 5.1, because it is the cut, light curve. One of the modeled transit events coincides with the available TESS sector 66. However, the modeled transit event was predicted to occur at $\mathrm{BJD} - 2450000 = 10107.954$ days, which is during a four-day data gap in that TESS sector.

The first and second observed transits are separated by $4 \cdot P = 742.51$ days. Moreover, there are $8 \cdot P = 1485.02$ days between the second and third observed transits. The proposed orbital period of the planet candidate listed on ExoFOP and the NASA exoplanet archive is $2 \cdot P = 742.51$ days. Because the intervals between the observed transits are integer subdivisions of the previously proposed period, the observed transit times are consistent with both that period, and integer subdivisions of that period. The RV analysis provides the additional information needed to rule out other periods than $P = 185.628$ days.

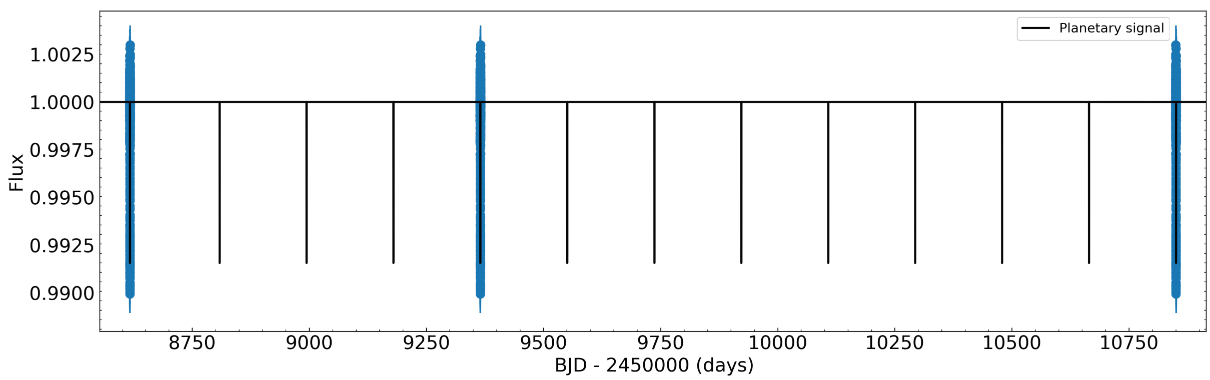

Figure 5.1: The observed transits in available 120 s cadence TESS light curve data (in blue) for TOI-1861, with the fitted model (in black).

As seen in the GLS RV periodogram in Figure 5.2, the only periodic signal in the RV data above both of the FAP levels corresponds to an orbital period of $P = 185.6$ days, which is one fourth of the previously proposed orbital period. This new orbital period is allowed by the observed transits in Figure 5.1 and implied by the RV periodogram, which grants it more plausibility in comparison to the orbital period on ExoFOP and the Exoplanet archive, $P = 742.51$ days, which was based solely on transit data alone. Moreover, the absence of peaks in Figure 5.3 suggests that the periodic signal is not a consequence of stellar activity.

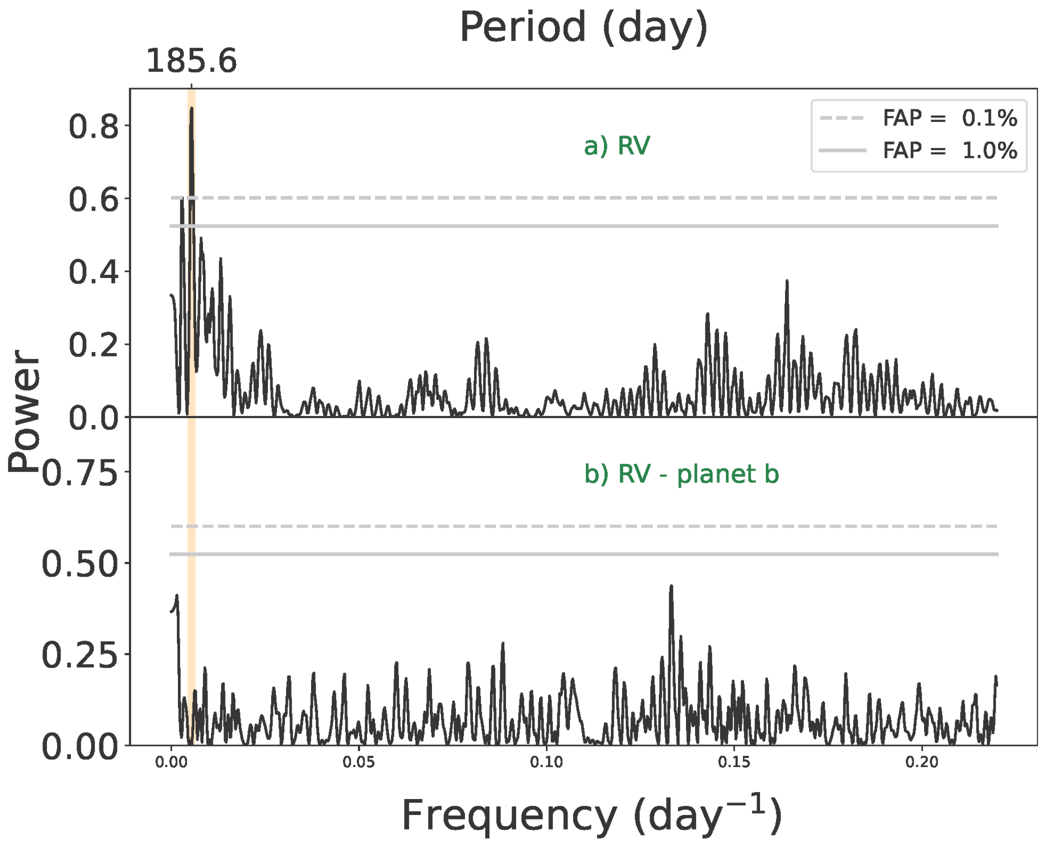

Figure 5.2: The GLS RV periodogram for TOI-1861. The highest peak is indicated by the vertical orange line. It corresponds to a periodic signal with a period of $P = 185.6$ days. The bottom panel is a periodogram of the residuals left after the periodic signal prominent in the upper panel was modeled and removed.

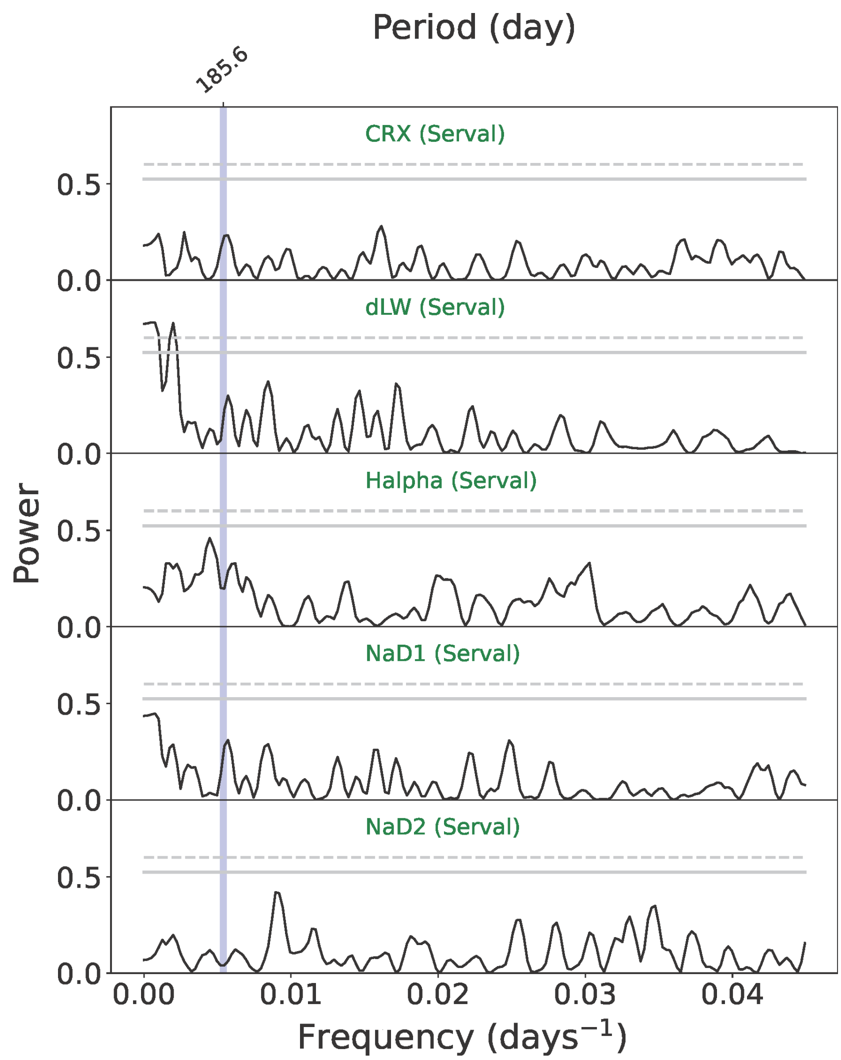

Figure 5.3: The GLS periodogram for five different stellar activity indicators for TOI-1861. The vertical blue line corresponds to $P = 185.6$ days.

5.1 Best-fitting Model

The measured RV time series, with the fitted model is shown in Figure 5.4. The periodic nature of the RV signal is clearly visible in the figure. However, for easier comparison between the model and the RV data, the phase folded RV time series along with the residuals of each data point is presented in Figure 5.5. The residuals are further discussed in section 6. Additionally, the phase folded light curve, along with the fitted model and the residuals is shown in Figure 5.6. The gray points are the unbinned data, while the blue represent a binned version of the same data. The model is depicted as a black line. The ingress and egress can clearly be seen, as well as a rounded, U-shaped bottom. A noteworthy characteristic is seen in the middle of the transit, where some data points are deviating from the model. The cause of which will be further discussed in section 6.

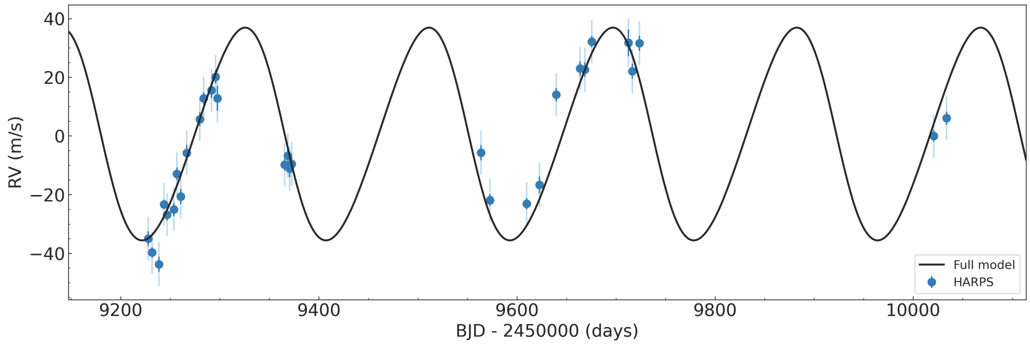

Figure 5.4: The RV time series for TOI-1861, with all RV data points extracted from HARPS spectra included (blue), along with the fitted model (black line).

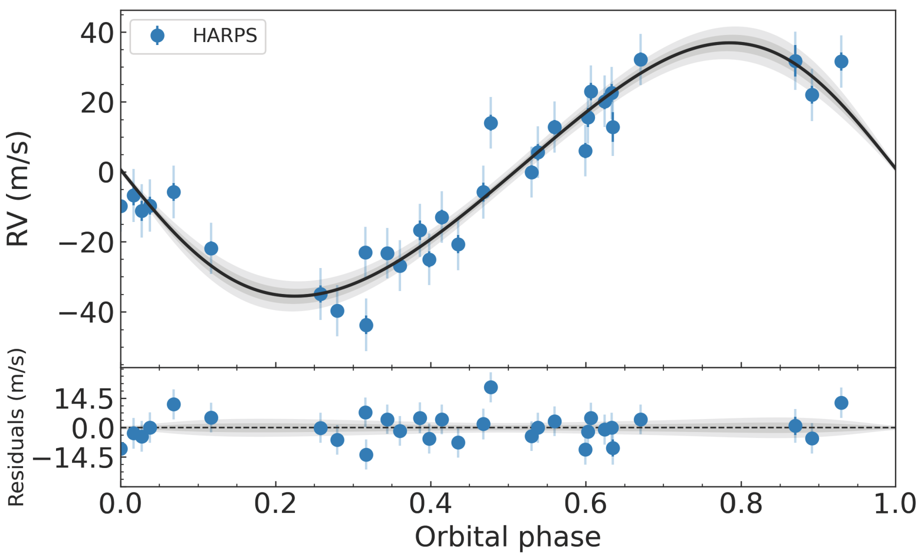

Figure 5.5: The folded RV time series for TOI-1861, along with the model (black line) and the residual of each data point.The gray regions represents the 68% credible interval of the fitted RV model.

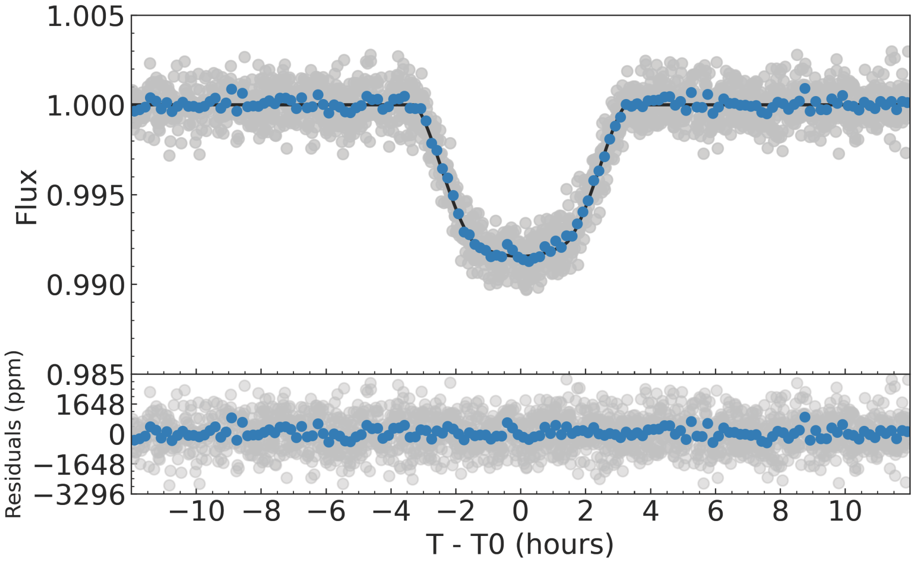

Figure 5.6: The folded light curve for TOI-1861, both unbinned (gray) and binned (blue) along with the model (black line) is shown above, with the residual of each data point included below.

Table 5.1: Best-fit transit and RV model parameters for TOI-1861.

Symbol	Parameter	Prior	Final value
Fitted parameters			
T_0	Transit epoch (- 2 450 000)	$\mathcal{U}[8622.9243, 8622.9293]$	8622.92643 ± 0.00076
$P_{\rm orb}$	Orbital period (d)	$\mathcal{U}[185.6185, 185.6385]$	185.6281 ± 0.0001
$ew1$	$\sqrt{e}\sin\omega$	$\mathcal{G}[0.3000, 0.0500]$	0.303 ± 0.04
$ew2$	$\sqrt{e}\cos\omega$	$\mathcal{G}[0.0600, 0.0500]$	0.060 ± 0.04
b	Impact parameter	$\mathcal{U}[0.01, 0.99]$	0.85 ± 0.01
$\rho_\star$	Stellar density (g/cm^3)	$\mathcal{G}[1.3, 0.2]$	$1.34^{+0.12}_{-0.11}$
$R_{\rm p}/R_\star$	Planet-to-star radius ratio	$\mathcal{U}[0.0866, 0.1066]$	$0.097^{+0.002}_{-0.001}$
K	Doppler semi-amplitude (m/s)	$\mathcal{G}[39.0, 5.0]$	$36.238^{+2.222}_{-2.174}$
Derived parameters			
$M_{\rm p}$	Planet mass ($\rm M_J$)	...	$1.017^{+0.11}_{-0.10}$
$R_{\rm p}$	Planet radius ($\rm R_J$)	...	0.998 ± 0.054
i	Inclination (deg)	...	$89.599^{+0.021}_{-0.023}$
a	Semi-major axis (AU)	...	$0.665^{+0.040}_{-0.039}$
e	Eccentricity	...	$0.097^{+0.025}_{-0.023}$
w	Angle of periastron (deg)	...	$78.9^{+8.1}_{-8.2}$
F	Insolation ($F_\oplus$)	...	$2.396^{+0.281}_{-0.254}$
$\rho_{\rm p}$	Planet density (g cm^{-3})	...	$1.265^{+0.272}_{-0.220}$
$g_{\rm p}$	Surface gravity^1 (cm s^{-2})	...	2533^{+409}_{-354}
$g_{\rm p}$	Surface gravity^2 (cm s^{-2})	...	2741^{+229}_{-218}
$T_{\rm eq}$	Equilibrium temperature (K)	...	$346.29^{+9.73}_{-9.57}$
TSM	Transmission spectroscopy metric	...	$0.782^{+0.108}_{-0.091}$
$\rho_\star$	Stellar density^3(g/cm^3)	...	$1.34^{+0.12}_{-0.11}$
$\rho_\star$	Stellar density^4(g/cm^3)	...	$1.19^{+0.26}_{-0.22}$
T_{14}	Total transit duration (h)	...	$6.5785^{+0.0695}_{-0.0653}$
T_{23}	Full transit duration (h)	...	$2.799^{+0.259}_{-0.261}$
Additional parameters			
γ	Systemic velocity (km/s)	...	-0.0124 ± 0.0014
σ	RV jitter (m/s)	...	$7.037^{+1.171}_{-0.944}$
q_1	$(u_1+u_2)^2$	$\mathcal{G}[0.3528, 0.2]$	$0.3998^{+0.137}_{-0.130}$
q_2	$\frac{u_1}{2(u_1+u_2)}$	$\mathcal{G}[0.3148, 0.2]$	$0.320^{+0.185}_{-0.171}$
Adopted stellar parameters			
$M_\star$	Stellar mass ($M_\odot$)	$\mathcal{F}$	1.010 ± 0.127
$R_\star$	Stellar radius ($R_\odot$)	$\mathcal{F}$	1.061 ± 0.055
$T_{\rm eff}$	Effective temperature (K)	$\mathcal{F}$	5684 ± 135

1: From planet parameters. 2: From K and $R_{\rm p}/R_\star$.
3: From transit. 4: From stellar parameters.

5.2 TOI-1861 b

The joint transit and RV analysis presented in this work confirms the planetary nature of TOI-1861 b and yields a mass of $1.0 \pm 0.1\, M_\mathrm{J}$, and a radius of $1.00 \pm 0.05\, R_\mathrm{J}$. The planet is therefore comparable to Jupiter in both mass and radius. However, with a considerably smaller semi-major axis, $a \approx 0.665\,\mathrm{AU}$ in comparison to Jupiter's semi-major axis, $a \approx 5.204\,\mathrm{AU}$, TOI-1861 b has a higher equilibrium temperature than Jupiter, and is hence categorized into the group warm Jupiters. Given its derived mass, radius and bulk density, it can be positioned into mass-radius as well as radius-density diagrams, included as Figure 5.7 and Figure 5.8. These diagrams plots all detected exoplanets with a mass and radius with uncertainties below 30 % and 10 % respectively. They also include theoretical composition models. Additionally, a logarithmic color bar indicating the instellation is included as well. TOI-1861 b is marked by a red star symbol. The planet TOI-1861 b falls on the theoretical hydrogen-helium planet composition.

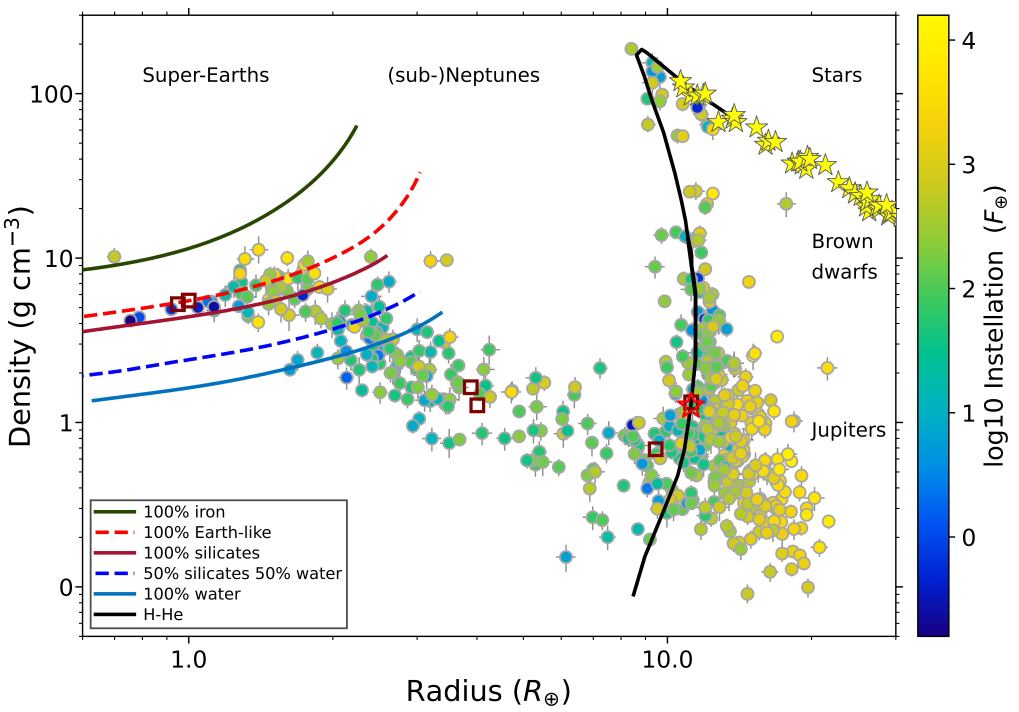

Figure 5.7: A radius-density diagram, with theoretical composition lines, as well as an instellation color bar (Zeng et al., 2016). TOI-1861 b is included and is indicated by a red star symbol.

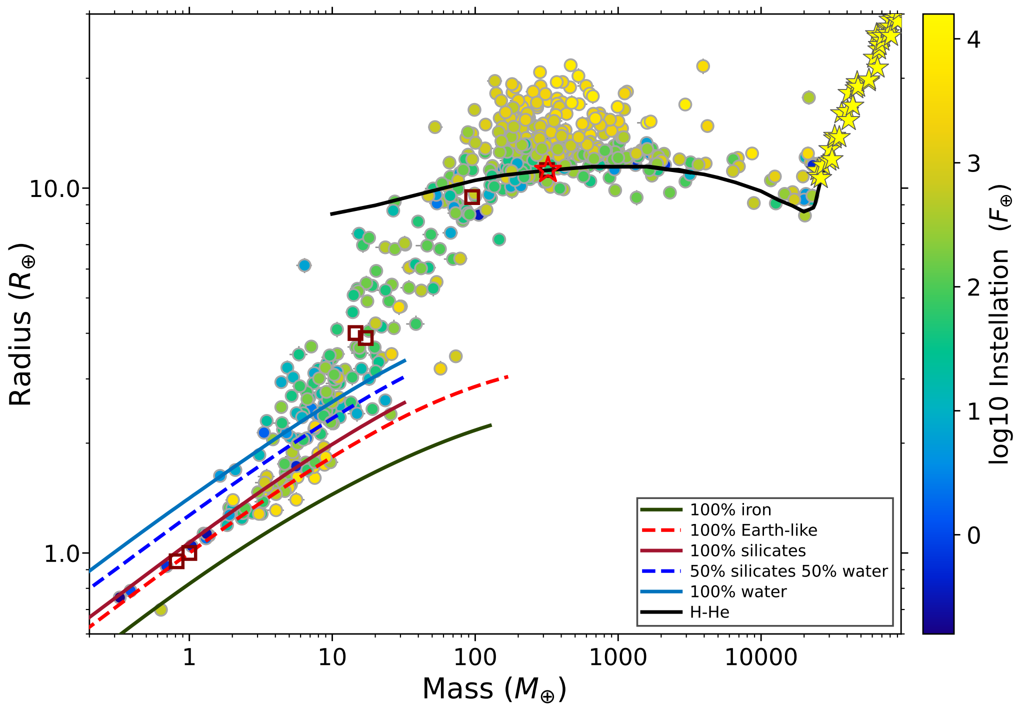

Figure 5.8: A mass-radius diagram, with theoretical composition lines, as well as an instellation color bar (Zeng et al., 2016). TOI-1861 b is included and is indicated by a red star symbol.

6 Discussion

6.1 The Model

In this work, joint RV and transit modeling was used to confirm and characterize TOI-1861 b, previously only a TESS-candidate. TOI-1861 b is a clear example showing the strength of combining the RV and transit detection methods to reliably confirm, and begin to characterize exoplanets. From the initial TESS observations, an orbital period of 742.51 days was inferred from the light curves following the three transit events detected. The now proposed shorter orbital period would not have been found, were it not for the supplementary RV analysis. The combination of the two data types reduce ambiguities and increase confidence in the physical parameters, and was in this case able to correct a previous mistaken conclusion.

The detection of TOI-1861 b is supported first of all through the consistent periodicity of the RV signal and the observed transits. Both the RV and transit data can be jointly reproduced with the proposed planetary parameters. Pyaneti uses a chi-squared measure, relative to the number of degrees of freedom in the model, to evaluate model performance. For the proposed parameters, a value of $\chi^2/(\text{degrees of freedom}) = 0.9508$ indicates that the residuals are broadly consistent with the assumed observational uncertainties.

The stellar density values from transits, as well as the stellar parameters are included in Table 5.1. Within their respective margins of error, the stellar densities are in agreement, which strengthens the reliability of the model. Finally, from a Bayesian statistical perspective, the posterior distributions from the model also forms a basis for analysis of the results. Generally, the model parameters show narrow Gaussian-like posteriors. Narrow Gaussian-like posterior distributions indicate that the parameters are relatively well constrained within the adopted model and prior assumptions.

6.2 The Residuals

Although many arguments can be made to support the detection of TOI-1861 b, there are some remaining questions to be addressed. Firstly, a number of RV measurements show relatively large residuals. A few single data points even deviate from the model as much as up to approximately 50% of the RV semi-amplitude. Given the arguments made previously that support the detection, this should not likely be interpreted as evidence against TOI-1861 b and its proposed parameters. Instead, other potential causes for these deviations were investigated as part of the work, but no clear conclusions were achieved in the end. Correlations were sought after in the relation between residual amplitude and signal-to-noise ratio of the observation, and also between residual amplitude and a number of weather-related parameters, but no correlation was ultimately found, and so the deviations could not be directly linked to any disturbance in the observing conditions. An explanation in the form of another planetary candidate or events linked directly to the host star were also considered. However, with no additional transit events, and no other strong periodic signal indicated from the RV-periodogram, the search for further planetary candidates is futile. Stellar activity indicators were also investigated as potential causes, again to no avail. Although, the absence of transits indicating an additional planet does not in itself rule out the possibility of another planet, because it could simply be non-transiting due to its inclination. Similarly, absence of RV signals indicating another planet does not rule out the possibility of another planet. Unfortunately, the origin of the largest residuals remains uncertain. Possible explanations include underestimated measurement uncertainties, instrumental systematics, stellar activity not traced by the analyzed activity indicators, or additional weak signals not captured by the current model.

6.3 Anomalous Feature in the Transit Light Curve

Finally, the folded transit light curve also contains an anomaly of sorts. At the very bottom of the transit, there is a sudden and brief increase of the flux. Although such features can be seen as a consequence of star spot crossings, it could also be explained by deviating data points, instrumental systematics, or the processing of the light curve. One possible explanation has not been analyzed further and is left for future discussions.

Bibliography

Anderson, D. R., et al. (2010). *WASP-30b: A 61 M_J BROWN DWARF TRANSITING A $V = 12$, F8 STAR*. The Astrophysical Journal Letters, 726(2), L19. DOI: `https://doi.org/10.1088/2041-8205/726/2/L19`

Barragán, O. (2022). *Citlalicue: Create and manipulate stellar light curves.* (ascl:2202.014). Astrophysics Source Code Library. URL: `https://ui.adsabs.harvard.edu/abs/2022ascl.soft02014B/abstract`

Barragán, O., et al. (2019). Pyaneti: A fast and powerful software suite for multi-planet radial velocity and transit fitting. *Monthly Notices of the Royal Astronomical Society*, *482*(1), 1017–1030. DOI: `https://doi.org/10.1093/mnras/sty2472`

Dawson, R. I., et al. (2018). *Origins of hot Jupiters.* Annual Review of Astronomy and Astrophysics, 56, 175–221. DOI: `https://doi.org/10.1146/annurev-astro-081817-051853`

de Pater, I., et al. (2015). *Planetary sciences.* (2nd ed.). Cambridge University Press. DOI: `https://doi.org/10.1017/CBO9781316165270`

Fulton, B. J., et al. (2017). *The California-Kepler Survey. III. A gap in the radius distribution of small planets.* The Astronomical Journal, 154(3), 109. DOI: `https://doi.org/10.3847/1538-3881/aa80eb`

Georgieva, I. (2023). *A Cosmic Quest for New Worlds: Characterising Exoplanet Signals via Radial Velocity and Transit Photometry* [Doctoral thesis, Chalmers University of Technology]. Chalmers Research. URL: `https://research.chalmers.se/publication/535808`

Hatzes, A. P. (2019). *The Doppler Method for the Detection of Exoplanets.* IOP publishing. DOI: `https://doi.org/10.1088/2514-3433/ab46a3`

Kipping, D. M. (2013). *Efficient, uninformative sampling of limb darkening coefficients for two-parameter laws.* Monthly Notices of the Royal Astronomical Society, 435(3), 2152–2160. DOI: https://doi.org/10.1093/mnras/stt1435

Lightkurve Collaboration, Cardoso, J. V. d. M., Hedges, C., et al. (2018). *Lightkurve: Kepler and TESS time series analysis in Python*. Astrophysics Source Code Library. URL: https://ui.adsabs.harvard.edu/search/q=author%3A%22Lightkurve%20Collaboration%22&sort=date%20desc%2C%20bibcode%20desc&p_=0

Mayor, M., et al. (1995). *A Jupiter-mass companion to a solar-type star*. Nature, 378(6555), 355-359. DOI: https://doi.org/10.1038/378355a0

Nordling, C., et al. (2006). *Physics handbook for science and engineering* (8th ed.). Studentlitteratur.

Perryman, M. (2018). *The Exoplanet Handbook*. (2nd ed.). Cambridge University Press. DOI: https://doi.org/10.1017/9781108304160

Petigura, E. A., et al. (2022). *The California-Kepler Survey. X. The radius gap as a function of stellar mass, metallicity, and age*. The Astronomical Journal, 163(4), 179. DOI: https://doi.org/10.3847/1538-3881/ac51e3

Ricker, G. R., et al. (2015). *Transiting Exoplanet Survey Satellite (TESS)*. Journal of Astronomical Telescopes, Instruments, and Systems, 1(1), 014003. DOI: https://doi.org/10.1117/1.JATIS.1.1.014003

Wolszczan, A., et al. (1992). *A planetary system around the millisecond pulsar PSR1257 + 12*. Nature, 355(6356), 145–147. DOI: https://doi.org/10.1038/355145a0

Zechmeister, M., et al. (2018). *Spectrum radial velocity analyser (SERVAL): High-precision radial velocities and two alternative spectral indicators*, *609*, A12. DOI: https://doi.org/10.1051/0004-6361/201731483

Zeng, L., et al. (2016). *Mass-radius relation for rocky planets based on PREM*. The Astrophysical Journal 819(2), 127. DOI: https://doi.org/10.3847/0004-637X/819/2/127

DEPARTMENT OF SOME SUBJECT OR TECHNOLOGY
CHALMERS UNIVERSITY OF TECHNOLOGY
Gothenburg, Sweden
www.chalmers.se

CHALMERS
UNIVERSITY OF TECHNOLOGY